CHEMISTRY OF MATERIALS

ARTICLE

pubs.acs.org/cm

In Situ High-Temperature Neutron Diffraction Study of A-Site Deficient Perovskites with Transition Metals on the B-Sublattice and Structure−Conductivity Correlation

Elena Konysheva* and John T. S. Irvine

School of Chemistry, University of St. Andrews, St. Andrews, Fife, KY 16 9ST, United Kingdom

Supporting Information

ABSTRACT: Neutron powder diffraction has been used for the first time to explore crystal structure and phase transformations in the Mn and Sr doped A-site deficient $La_{0.95}Ni_{0.6}Fe_{0.4}O_3$ (LSNFM series) as a function of temperature and upon different doping regimes. The range of A-site deficiency in the simple perovskite structure with Ni, Fe, and Mn cations on the B-sublattice is very low, and all the A-site deficient nominal compositions explored can be represented as a mixture of the cation stoichiometric perovskite phase with rhombohedral structure and NiO as a secondary phase in the temperature range of 45−460 °C. The *a* lattice parameter and the unit cell volume of the perovskite phase in the LSNFM compositions increase upon Sr and Mn doping. Exsolution of NiO from the perovskite phase in the Mn doped $La_{0.95}Ni_{0.6}Fe_{0.4}O_3$ with the rise in the temperature was stronger compared to that in the LSNFM compositions with a low level of Sr doping ($0.004 \le x \le 0.042$). The local distortions of the $[NiO_6]$ octahedra, existing most probably due to the mismatch in the $Ni^{3+}-O$ and $Ni^{2+}-O$ bond lengths, seems to be compensated through the incorporation of Sr cations with a larger ionic radius onto the A-sublattice of the perovskite phase. Reversible high-temperature phase transition from rhombohedral ($R\bar{3}c$) to cubic ($Pm\bar{3}m$) symmetry occurs above 530−600 °C within the cation stoichiometric perovskite phase in all the A-site deficient compositions. The increase in the degree of Sr substitution in the LSNFM series diminishes the high temperature phase transition within the cation stoichiometric perovskite phase. The change in the conductivity of the Mn and Sr substituted compositions at room temperature can be explained through the increase in the lattice parameters of the perovskite phase. At high temperatures there is no correlation between the evolution of the phase equilibria and the transport properties of the compositions in the LSNFM series. Mechanism of the band formation and variation of its components with the temperature have been discussed.

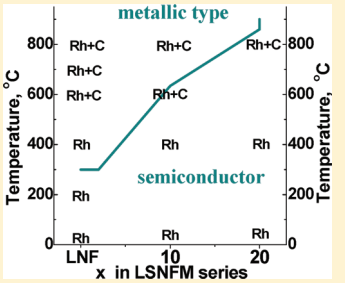

KEYWORDS: in situ neutron diffraction, A-site deficiency, perovskites, high temperature phase transition, electronic conductivity

1. INTRODUCTION

Recently A-site deficient perovskites have attracted more and more attention because of good electrochemical characteristics, better thermal stability, and chemical compatibility with other components in solid state devices for power generation.[1−7] Limited structural characterization studies, however, have been carried out so far for this group of materials.[8−13] According to X-ray diffraction, the A-site deficient nominal compositions $(La_{0.75}Sr_{0.25})_{0.95}Cr_{0.5}Mn_{0.5}O_3$[8] and $(La_{1-x}Sr_x)_yFeO_{3+\delta}$ ($0.2 \le x \le 0.5$ and the average A-site occupancy between $0.8 \le y \le 1.0$)[9] were originally determined as pure perovskite phases. The presence of (Cr,Mn)spinel and $SrFe_{12}O_{19}$ as the secondary phases in the $(La_{0.75}Sr_{0.25})_{0.95}Cr_{0.5}Mn_{0.5}O_3$[8] and $(La_{1-x}Sr_x)_y$-$FeO_{3+\delta}$,[9] respectively, has emerged from the application of neutron powder diffraction and high-energy synchrotron radiation. Minor phase development was observed in $La_{0.8}Sr_xMnO_3$ ($x = 0-0.45$) by X-ray powder diffractometry, scanning electron microscopy, transmission electron microscopy, and energy-dispersive X-ray emission spectroscopy.[10] In the case of the A-site deficient $La_yNi_{0.6}Fe_{0.4}O_3$, the two very weak diffraction peaks related to NiO were found in the XRD pattern recorded at room temperature in the reflection mode before and after calcination at high temperature.[5,13] The use of neutron powder diffraction allowed the characterization of NiO as a secondary phase in A-site deficient nominal composition $La_{0.95}Ni_{0.6}Fe_{0.4}O_3$ structurally and quantitatively.[11] The above-mentioned experimental findings cast doubt on the range and perhaps existence of the A-site deficiency in the simple perovskite structure containing Ni, Fe, and Mn transition metals onto the B-sublattice, although this is of great importance for the designing of new materials with the required functional properties. A-site deficiency in simple oxides is well-known and can result in formation of cation vacancies on the A sublattice, rather than formation of an impurity phase, due to the compensation of the A-site vacancy by oxidation of the B sublattice or oxygen vacancy formation. The existence of Ni vacancies in a $Ni_{1-y}O$ film with the cation deficiency in the range of $0 < y < 0.2$ was reported in the literature.[14] According to the theoretical studies, the surface layer of nickel oxide is enriched in Ni vacancies by about a factor of 40.[15] The existence of cation vacancies onto the A sublattice was also demonstrated for more

Received: December 7, 2010
Revised: February 26, 2011
Published: March 15, 2011

complex structures, such as bronzes, $La_{1/3}NbO_3$, $La_{1/3}TaO_3$, and $La_{2/3}TiO_3$.[16−18]

The full structural complexity of complex oxides cannot be revealed only by X-ray diffraction. High-temperature phase transitions have been reported recently for cation-stoichiometric simple perovskites ($CaTiO_3$,[19] $BaCeO_3$,[20] $La_{0.9}Sr_{0.1}Ga_{0.8}Mg_{0.2}O_{2.85}$,[21] $La_{0.75}Sr_{0.25}Cr_{0.5}Mn_{0.5}O_{3-\delta}$,[8] and $Pr_{1-x}Sr_xMnO_3$[22]) and for double perovskites Sr_2MWO_6 (M = Ni, Zn, Co, Cu).[23] The second order high-temperature phase transition $R\bar{3}c \leftrightarrow Pm\bar{3}m$ was revealed for the cation stoichiometric perovskite phase in the A-site deficient $La_{0.95}Ni_{0.6}Fe_{0.4}O_3$.[11] Apart from $La_{0.95}Ni_{0.6}Fe_{0.4}O_3$, the existence of the high temperature perovskite phase with cubic symmetry in the La−Sr−Ni−Fe−Mn−O system was reported for the oxygen deficient $SrMnO_{3-\delta}$ (300−900 °C)[24] and for $SrFeO_3$ (above 580 °C under high oxygen pressure).[25] At room temperature in air the existence of a perovskite with cubic symmetry was revealed for the fully oxidized $SrFeO_3$, whereas $SrFeO_{3-\delta}$ with brownmillerite structure ($0.25 \le \delta \le 0.5$) is formed on heating.[26] A- and B-site substituted solid solutions $La_{1-x}Sr_xCo_{1-y}Fe_yO_{3-\delta}$ and $La_{1-x}Sr_xCo_{1-y}Ni_yO_{3-\delta}$ with $x > 0.5$ have an ideal cubic structure at room temperature ($Pm\bar{3}m$).[27,28]

The present investigation aims to carry out in situ high-temperature structural characterization of $La_{0.95}Ni_{0.6}Fe_{0.4}O_3$ modified by small additions of $La_{0.8}Sr_{0.2}MnO_3$ and MnO_2, exploring the effect of the Sr and Mn substitution on phase equilibria, crystal structure of the perovskite constituent, and NiO exsolution. This investigation also aims to specify whether there are any correlations between the phase/structural evolution and the transport properties at intermediate temperatures in the La−Sr−Ni−Fe−Mn−O system. It is known that $LaNi_{0.6}Fe_{0.4}O_{3-\delta}$ perovskite has the highest electronic conductivity in the $LaNi_{1-y}Fe_yO_{3-\delta}$ series and it has been considered as a cathode material for the application in solid oxide fuel cells. $LaNi_{0.6}Fe_{0.4}O_{3-\delta}$ shows metallic conductivity at a temperature higher than 300 °C.[1,12] Temperature of the semiconducting−metallic transition and the total conductivity can be varied through doping.

2. EXPERIMENTAL SECTION

2.1. Sample Preparation. The initial compositions $La_{0.8}Sr_{0.2}MnO_3$ (99.9%) and $La_{0.95}Ni_{0.6}Fe_{0.4}O_3$ (99.9%) (LNF) produced by combustion spray pyrolysis were supplied by PRAXAIR Inc., USA. MnO_2 (99.9%) was delivered by ALFA AESAR (Lancashire, U.K.). The compositions $La_{0.931}Ni_{0.588}Fe_{0.392}Mn_{0.02}O_3$ (LNFM02), $La_{0.947}Sr_{0.004}Ni_{0.588}Fe_{0.392}Mn_{0.02}O_3$ (LSNFM02), $La_{0.935}Sr_{0.02}Ni_{0.54}Fe_{0.36}Mn_{0.1}O_3$ (LSNFM10), and $La_{0.92}Sr_{0.04}Ni_{0.48}Fe_{0.32}Mn_{0.2}O_3$ (LSNFM20) were obtained by mechanical mixing of LNF and $La_{0.8}Sr_{0.2}MnO_3$ or MnO_2 (Supporting Information) followed by calcination in air at 1350 °C for 5 h. The initial LNF was also calcined under the same conditions. Possible contamination of the samples by carbon was checked by using an elemental analyzer 1110 CHNS CE Instrument (ThermoQuest Italia S.P.A, Rodano, Italy).

2.2. Characterization Methods. Neutron powder diffraction (NPD) measurements were carried on the D1A instrument, using a wavelength of $\lambda = 1.909$ Å (ILL, Grenoble, France). Measurements were carried out in a temperature range of 25−800 °C under air in a quartz tube for all the compositions investigated. The diffraction data were registered in the angular range $0 \le 2\Theta \le 158°$ with a step size of 0.05°. The diffraction data were refined by the Rietveld method,[29] using the program General Structure Analysis System (GSAS).[30] X-ray powder diffraction (XRD) data were recorded in air at room temperature (RT) in reflection mode on a Philips analytical X-ray PW1710 diffractometer with Cu Kα radiation (Nederlandse Philips Bedrijven B.V., The Netherlands) to identify impurities. Thermal gravimetric analysis (TGA) was carried out on NETZSCH TG 209 instrument (NETZSCH-Geraetebau GmbH, Selb, Germany) with a heating/cooling rate of 5 °C/min to evaluate the oxygen loss and accommodation on thermal cycling in air in the compositions synthesized.[31] The dilatometry investigation was carried out on a NETZSCH DIL 402C dilatometer (alumina holder) with a TASC 414/4 controller. The pellets with a relative density of about 90−93% were tested in air on cooling in the temperature range of 25−900 °C at a rate of 3 °C/min. In addition, the two consecutive thermal cycles were carried out with LSNFM10 and LSNFM20. Electrical conductivity was measured on the sintered pellets by the standard four terminal DC method between 25 and 900 °C in ambient air, using a heating and cooling rate of 1−2 °C/min. A current of 100 mA (model: Keithley 220, Keithley Instruments Inc., U.S.A.) was applied in both directions, and resistance was calculated as a gradient of potential vs current. This was converted to conductivity using the geometrical factor of the sample. Au paste (T10112, Metalor Technologies Ltd., U.K.) was applied as an electrode to improve contact between samples and current/potential probes.[13]

Table 1. Comparison of the Nominal A-Site Deficiency in the Compositions Explored and the Fraction of NiO Defined from the Refinement of the NPD Patterns

A-site deficient nominal composition	nominal A-site deficiency, mol %	fraction of NiO obtained from the refinement, mol %
LSNFM20	4	4.3 ± 0.1
LSNFM10	4.5	4.7 ± 0.1
LSNFM02	4.9	5.3 ± 0.1
LNF[a]	5	5.2 ± 0.1
LNFM02	6.9	7.1 ± 0.3

[a] Data from ref 11.

3. RESULTS AND DISCUSSION

3.1. Phase Composition and Structure at Near Room Temperature. All the A-site deficient compositions LNFM02, LSNFM02, LSNFM10, and LSNFM20 at room temperature have rhombohedral structure according to X-ray diffraction recorded in the transmission mode.[12,13] The two weak peaks related to NiO (and not to Mn oxides or spinels) were revealed in the XRD patterns recorded in the reflection mode for these compositions (Figure 1a). Neutron powder diffraction analysis (NPD) carried out at near room temperature confirmed the presence of only NiO as a secondary phase (six clearly distinguished diffraction peaks) (Figure 1b,c). Any peaks related to manganese oxides or manganese containing compounds were not observed in the NPD pattern of LNFM02 fabricated through the mixing of LNF and MnO_2, implying that the Mn cations replace more reducible Ni onto the B sublattice of the perovskite lattice. Ni cations exsolve from the perovskite structure and segregate as a secondary phase, further increasing the concentration of NiO. Similar effect was observed for $La_{0.95}Ni_{0.6}Fe_{0.4}O_3$ containing small additions of TiO_2.[12] No additional scattering peaks that could be magnetic in origin were observed in the NPD patterns recorded for the LSNFM compositions. The fractions of NiO as a secondary phase obtained from the refinement are very close to the nominal A-site deficiency in LNFM02, LSNFM02, LSNFM10, LSNFM20, and LNF (Table 1), indicating that there is no A-site deficiency in these perovskites or its range is very low.

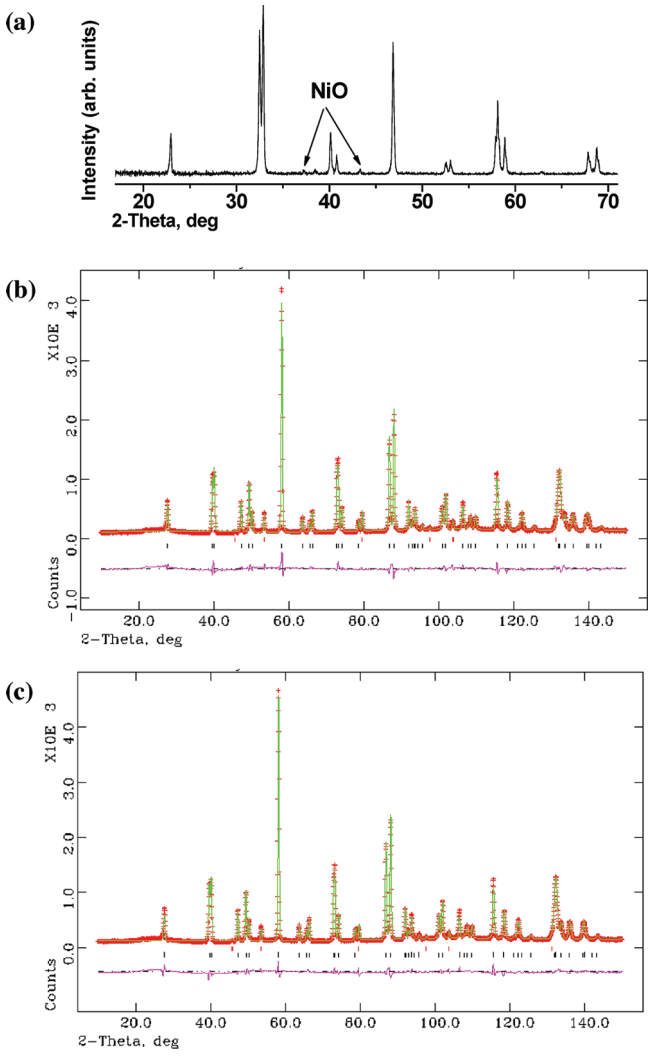

Figure 1. (a) X-ray powder diffraction pattern of the LNFM02 recorded in the reflection mode at 25 °C; (b) neutron diffraction pattern of the LNFM02 at 60 °C (R_{wp} = 7.26%, R_p = 6.27%, χ^2 = 1.67); (c) neutron diffraction pattern of the LSNFM02 at 45 °C (R_{wp} = 6.91%, R_p = 5.70%, χ^2 = 1.73): observed (cross symbols), calculated (continuous line), and difference profiles (bottom line). Vertical bars show calculated reflections for different phases: upper, NiO; lower, cation stoichiometric composition with rhombohedral symmetry ($R\bar{3}c$, No. 167).

Further all the compositions investigated in the present study were presented at room temperature as a mixture of the cation stoichiometric perovskite phase and NiO.

B-site occupancy in the stoichiometric perovskite phase cannot be refined with sufficient accuracy. First of all, it is not possible to refine the occupancies of three cations on one site with one set of neutron data. Another reason is the small difference in the neutron scattering lengths of Ni and Fe (10.3 fm and 9.45 fm, respectively) and a low concentration of Mn cations on the B sites, although the neutron scattering length of Mn is different and negative (−3.73 fm).[32] For instance, the Mn occupancy was fixed to 0.021, but the refinement carried out for LNFM02 confirmed insufficient accuracy of the B-site occupancy in the perovskite constituent: 0.623(43) for Ni, 0.356(43) for Fe. When the occupancies of all three cations were varied the errors of the refinement became several times higher than the values of the occupancies. Therefore, the Ni/Fe/Mn ratios in the corresponding stoichiometric perovskite phases were fixed accordingly. The final refined structural parameters for the A-site deficient nominal compositions are listed in Table 2. The cation stoichiometric perovskites in LNFM02 and LSNFM compositions exhibit rhombohedral structure: space group $R\bar{3}c$ (No. 167), with La/Sr in 2(a), Ni/Fe/Mn in 2(b), and O in 6(e) sites. The unit cell of NiO was refined as rhombohedral with space group $R\bar{3}m$ (No. 166), with Ni in 1(a) and O in 1(b) sites.

A low level of Mn doping (z = 0.021) results in the increase in the lattice parameters and unit cell volume of the perovskite phase: a = 5.4526(1) Å, β = 60.740(1)°, V = 116.544(2) Å^3, Z = 2 (in LNFM02), and a = 5.4491(1) Å, β = 60.761(1)°, V = 116.372(3) Å^3, Z = 2 (in LNF[11]). It was reported in the literature that the average oxidation state of the Ni cations tends to reduce with Mn substitution ($La^{3+}Ni^{2.74+}_{0.75}Mn^{3.77+}_{0.25}O_{3.0}$)[33] through the double exchange mechanism.[34] However, the perovskite phases in LNFM02 and LSNFM02 have close lattice parameters (Table 2), demonstrating that a very low level of Sr doping (x = 0.004) influences slightly the structural parameters. The a lattice parameter and the unit cell volume of the cation stoichiometric perovskite phase increase upon further doping with Sr and Mn in the LSNFM series and obey the Vegard's law (Table 2). In the case of the simultaneous Sr (x = 0.021 and 0.042) and Mn doping (z = 0.105 and 0.208), the increase in the unit cell volume of the substituted perovskite phases could be related to two processes: the increase in the concentration of Sr cations with a lager ionic radius and the rise in the fraction of Ni^{n+} cations with n < 3+ (with a lager ionic radius[35]) that emerged due to the Mn doping.

3.2. Phase Composition and Structure in the A-Site Deficient LNFM02 and LSNFM02 as a Function of Temperature. Figure 2 illustrates the development of the NPD patterns of LNFM02 and LSNFM02 (range 2Θ: 38.2−40.9°) as a function of temperature. The rhombohedral distortion decreases with the rise in the temperature. The change in the space group symmetry of the rhombohedral phase from $R\bar{3}c$ to $R3c$ (No. 161) or from $R\bar{3}c$ to $R\bar{3}$ (No. 148) does not occur at 450−460 °C (Table 3). The $R\bar{3}c$/NiO phase ratio was not fixed during the refinement. NiO concentration remains nearly constant in LSNFM02, whereas it increases up to 8.5 mol % in LNFM02, thereby illustrating that a very low level of Sr doping prevents NiO exsolution from the perovskite structure. The exsolution of NiO with the temperature variation was also observed for LNF.[11] The nominal LNFM02 composition can be represented as a mixture of NiO and $LaNi_{0.546}Fe_{0.421}Mn_{0.021}O_3$, formally introducing B-site deficiency within the perovskite phase (R_{wp} = 6.85%, R_p = 5.85%, χ^2 = 1.35). La_2O_3 or related phases were not observed in the NPD pattern. Further refinement of the La site occupancy indicates that slightly better reliability factors and χ^2 can be obtained for a composition with La site occupancy lower than 1 and proportional to the sum of Ni, Fe, and Mn site occupancies (R_{wp} = 6.69%, R_p = 5.68%, χ^2 = 1.32). The final refinement of the NPD patterns recorded for LNFM02 at 460 °C and for LSNFM02 at 450 °C was carried out as for the mixture of a cation stoichiometric phase and NiO with the two phase model {$R\bar{3}c$/NiO} (Table 2).

The NPD patterns obtained for LNFM02 and LSNFM02 at 800 °C were refined with different models: the {$R\bar{3}c$/NiO} two phase model, the {$R3c$/NiO} two phase model, the {$Pm\bar{3}m$/NiO} two phase model, the combined {$R\bar{3}c$/$Pm\bar{3}m$/NiO} three phase model, and the combined {$R3c$/$Pm\bar{3}m$/NiO} three phase model. The choice of the models for the refinement of the NPD

dx.doi.org/10.1021/cm103486z |Chem. Mater. 2011, 23, 1841–1850

Table 2. Refined Structure Parameters[a]

		LNFM02				LSNFM02				LSNFM10	LSNFM20
atom	parameter	60 °C	460 °C	800 °C		45 °C	450 °C	800 °C		45 °C	45 °C
						perovskite constituent					
		$R\bar{3}c$	$R\bar{3}c$	$R\bar{3}c$	$Pm\bar{3}m$	$R\bar{3}c$	$R\bar{3}c$	$R\bar{3}c$	$Pm\bar{3}m$	$R\bar{3}c$	$R\bar{3}c$
La/Sr	U_{iso} (Å^2)	0.0033(5)	0.0116(4)	0.0110(4)	0.096(8)	0.0047(4)	0.0122(23)	0.0162(4)	0.114(7)	0.0074(5)	0.0055(9)
occupancy	La	1	1	1	1	0.996	0.996	0.996	0.996	0.979	0.958
	Sr	0	0	0	0	0.004	0.004	0.004	0.004	0.021	0.042
Ni/Fe/Mn	U_{iso} (Å^2)	0.0026(4)	0.0067(4)	0.0041(3)	0.038(4)	0.0043(4)	0.0079(19)	0.0108(3)	0.020(2)	0.0007(4)	0.0005
occupancy	Ni	0.558	0.553	0.548	0.548	0.567	0.567	0.562	0.562	0.518	0.459
	Fe	0.421	0.426	0.430	0.430	0.412	0.412	0.417	0.417	0.377	0.333
	Mn	0.021	0.021	0.022	0.022	0.021	0.021	0.021	0.021	0.105	0.208
O	x	0.6976(2)	0.7009(2)	0.7040(3)	0	0.6972(3)	0.7004(9)	0.7047(2)	0	0.6981(3)	0.6971(2)
	y	−0.1976(2)	−0.2009(2)	−0.2040(3)	1/2	−0.1972(3)	−0.2004(9)	−0.2047(2)	1/2	−0.1981(3)	−0.1971(2)
	z	1/4	1/4	1/4	1/2	1/4	1/4	1/4	1/2	1/4	1/4
	U_{iso} (Å^2)	0.0077(4)	0.0169(4)	0.0200(3)	0.087(6)	0.0100(3)	0.0173(15)	0.0264(3)	0.102(6)	0.0116(3)	0.0095(7)
occupancy	O	0.996(3)	0.990(3)	1	1	0.995(3)	0.988(3)	1	1	0.997(3)	0.973(3)
a, (Å)		5.4526(1)	5.4859(1)	5.5161(1)	3.9166(6)	5.4524(1)	5.4858(1)	5.5169(1)	3.9168(5)	5.4553(1)	5.4579(1)
β (deg)		60.740(1)	60.566(1)	60.418(1)	90	60.755(1)	60.563(1)	60.411(1)	90	60.735(1)	60.737(1)
V, (Å^3)		116.544(2)	118.237(4)	119.804(2)	60.08(3)	116.566(2)	118.222(2)	119.834(1)	60.09(2)	116.707(2)	116.878(2)
						NiO					
		$R\bar{3}m$	$R\bar{3}m$	$R\bar{3}m$		$R\bar{3}m$	$R\bar{3}m$	$R\bar{3}m$		$R\bar{3}m$	$R\bar{3}m$
Ni	U_{iso} (Å^2)	0.0002	0.0044	0.0181(19)		0.0002	0.0044	0.020(3)		0.0002	0.0002
occupancy		1	0.919(13)	0.967(4)		0.97(2)	1	0.99(1)		1	1
O	U_{iso} (Å^2)	0.0002	0.0030	0.0147(32)		0.0002	0.0030	0.0104(42)		0.0002	0.0002
occupancy		1	1	1		1	1	1		1	1
a, (Å)		2.9535(9)	2.9734(4)	2.9869(6)		2.9560(5)	2.9726(4)	2.9888(3)		2.9560(1)	2.9587(13)
β (deg)		59.99(1)	60.01(1)	60.07(2)		59.99(1)	60.03(1)	60.07(1)		60.00(5)	59.95(4)
V, (Å^3)		18.251(2)	18.593(4)	18.874(3)		18.260(2)	18.587(3)	18.908(2)		18.264(4)	18.293(7)
R_{wp} (%)		7.26	5.83	5.41		6.91	6.76	5.57		7.81	7.50
R_p (%)		6.27	4.96	4.75		5.70	5.69	4.70		6.38	5.95
χ^2		1.67	1.20	1.00		1.73	1.50	1.01		2.43	1.708

[a] (x, y, z) coordinates of atoms in the cation stoichiometric perovskite with rhombohedral symmetry ($R\bar{3}c$): La/Sr (1/4, 1/4, 1/4) and Ni/Fe/Mn (0, 0, 0); the cation stoichiometric perovskite with cubic symmetry ($Pm\bar{3}m$): La/Sr (0, 0, 0) and Ni/Fe/Mn (1/2, 1/2, 1/2); NiO with rhombohedral symmetry ($R\bar{3}m$): Ni (0, 0, 0) and O (1/2, 1/2, 1/2).

dx.doi.org/10.1021/cm103486z |*Chem. Mater.* 2011, 23, 1841–1850

patterns was governed by the following factors. The splitting of the peak at about 38.2−40.8° decreases further compared to that at 450−460 °C (Figure 2). At 800 °C the peaks in the NPD patterns of LNFM02 and LSNFM02 have an asymmetrical form (Figure 2), thereby implying the appearance of a new phase with higher symmetry. The gradual decrease in the splitting could also indicate that a second order transformation takes place, as was observed for LNF.[11] The only transformation that will meet the requirements: for a second order transformation to higher symmetry is $R\bar{3}c \rightarrow Pm\bar{3}m$, although several symmetry transformations could occur within the $R\bar{3}c$ perovskite structure according to the group−subgroup relationships ($R\bar{3}c \rightarrow Pm\bar{3}m$, $R\bar{3}c \rightarrow I2/a \rightarrow I4/mcm$ or $R\bar{3}c \rightarrow C2/c$) depending on the tilting of the anion octahedra, distortion of the octahedral cage, or off-centering of the octahedrally coordinated cation or the 12-fold coordinated A-site.[36−39] The reliability factors and χ^2 obtained for the two and combined three phase models are presented in Tables 2 and 3. For both LNFM02 and LSNFM02, the best reliability factors and χ^2 were achieved when the combined {$R\bar{3}c$/$Pm\bar{3}m$/NiO} three phase model was used for the refinement (Table 2), although the accuracy of the refinement for the {$R\bar{3}c$/NiO} two phase model and the {$R3c$/NiO} two phase model (for LSNFM02 only) was slightly worse (Table 3). Compared to the {$R\bar{3}c$/NiO} and {$R3c$/NiO} models, the total number of variable parameters in the {$R\bar{3}c$/$Pm\bar{3}m$/NiO} model is more,

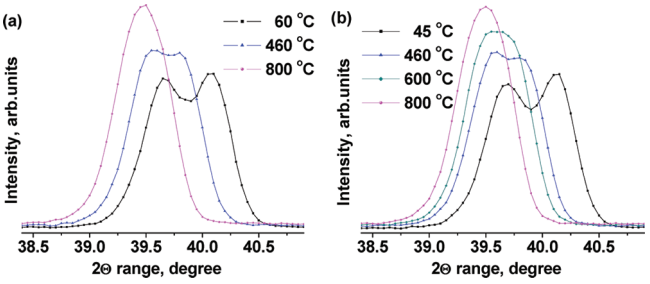

Figure 2. Evolution of neutron diffraction patterns of the (a) LNFM02 and (b) LSNFM02 as a function of the temperature.

and a small decrease in the reliability factors (R_{wp} and R_p) and χ^2 observed for this model can be considered as a significant improvement of the refinement carried out. According to the preliminary refinement, the fraction of NiO in LNFM02 at 800 °C increases further up to 8.9 mol %, whereas in LSNFM02 it rises slightly up to 5.9 mol % (compared to 5.3 mol % at 45 °C). Any peaks related to La_2O_3 or another La containing phase were not revealed in the NPD patterns. The reliability factors and χ^2 were better if the perovskite constituents did not exhibit deviation from the cation stoichiometry. Therefore, the final refinement of the NPD pattern obtained at 800 °C for LNFM02 and LSNFM02 was carried out for the mixture of the cation stoichiometric perovskite phases ($R\bar{3}c$ and $Pm\bar{3}m$) and NiO with the combined {$R\bar{3}c$/$Pm\bar{3}m$/NiO} three phase model (Tables 2 and 3 and Figure 3). It should be mentioned that in general La and Sr redistribution between the perovskite phases with rhombohedral and cubic symmetries could occur at high temperatures within the same A-site deficient nominal composition and facilitate the high-temperature phase transition within the cation stoichiometric perovskite phase. This, however, was not possible to specify from the refinement because the difference in the neutron scattering lengths of La and Sr (8.24 fm and 7.02 fm, respectively) is not so large and the concentration of Sr is low.

The high temperature phase has cubic symmetry $Pm\bar{3}m$ (No. 221), with La/Sr in 1(a), Ni/Fe/Mn in 1(b), and O in 3(e). The structural parameters for the perovskite constituent with cubic symmetry ($Pm\bar{3}m$) in LNFM02 and LSNFM02 are similar at 800 °C (Table 2).

3.3. Comparison of the Phase Composition and Structure in the LSNFM System. The procedure described in the previous sections was applied for the refinement of the NPD patterns recorded for the A-site deficient LSNFM10 and LSNFM20 compositions at 45 °C, 400 °C, and 800 °C. Data for all the compositions are summarized in Figures 4−8 and in Table 2.

The fraction of the cation stoichiometric perovskite phase with rhombohedral structure ($R\bar{3}c$) decreases, whereas that of the perovskite phase with cubic symmetry ($Pm\bar{3}m$) increases above 400 °C for all the compositions in the LSNFM series (Figure 4).

Table 3. Comparison of the Refinements with Different Models of the NPD Patterns Obtained at 450−460 and 800 °C for the LNFM02 and LSNFM02

				reliability factors[a]		
composition	temperature, °C	$\frac{[La]+[Sr]}{[Ni]+[Fe]+[Mn]}$ ratio	phase model	R_{wp}, %	R_p, %	χ^2
LNFM02	460	$\frac{1+0}{0.553+0.426+0.021}$	{$R3c$/NiO}	11.75	8.40	2.32
			{$R\bar{3}$/NiO}	203.90	23.02	11.55
	800	$\frac{1+0}{0.558+0.430+0.022}$	{$R\bar{3}c$/NiO}	5.94	5.27	1.14
			{$R3c$/$Pm\bar{3}m$/NiO}	21.95	16.93	5.68
			{$R3c$/NiO}	29.02	21.63	9.15
			{$Pm\bar{3}m$/NiO}	42.85	34.18	18.06
LSNFM02	450	$\frac{0.996+0.004}{0.567+0.412+0.021)}$	{$R3c$/NiO}	16.10	11.67	4.10
			{$R\bar{3}$/NiO}	33.29	27.57	11.41
	800	$\frac{0.996+0.004}{0.562+0.417+0.021)}$	{$R\bar{3}c$/NiO}	7.12	5.79	1.34
			{$R3c$/$Pm\bar{3}m$/NiO}	12.52	8.40	2.60
			{$R3c$/NiO}	11.89	8.05	2.18
			{$Pm\bar{3}m$/NiO}	41.77	32.41	19.03

[a] Reliability factors are presented after the subtraction of the background.

dx.doi.org/10.1021/cm103486z |Chem. Mater. 2011, 23, 1841–1850

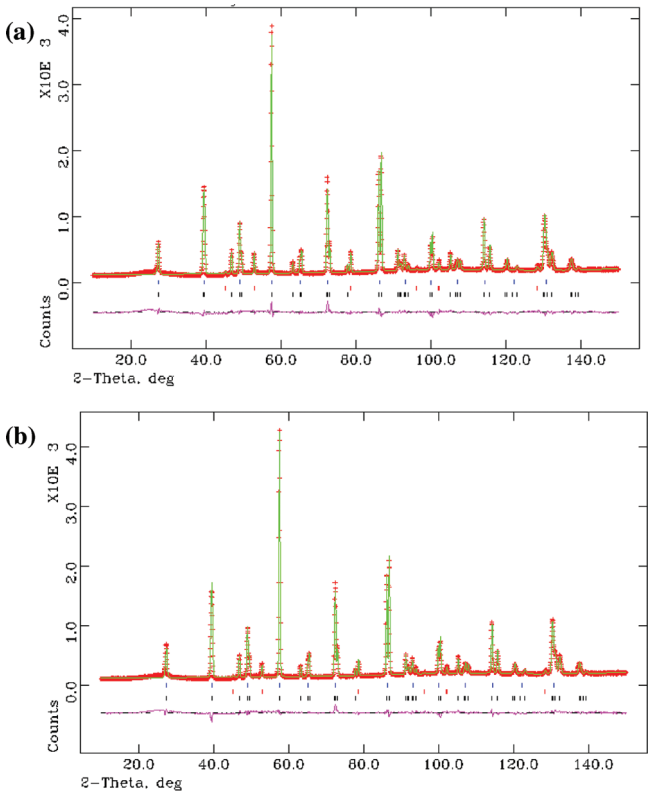

Figure 3. Neutron diffraction patterns at 800 °C for the (a) LNFM02 (R_{wp} = 5.41%, R_p = 4.75%, χ^2 = 1.00) and (b) LSNFM02 (R_{wp} = 5.57%, R_p = 4.70%, χ^2 = 1.01): observed (cross symbols), calculated (continuous line), and difference profiles (bottom line). Vertical bars show calculated reflections for different phases: upper, perovskite phase with cubic symmetry ($Pm\bar{3}m$, No. 221); middle, NiO; and lower, perovskite phase with rhombohedral symmetry ($R\bar{3}c$, No. 167).

The normalized unit cell volumes of the cation stoichiometric perovskite phases with rhombohedral symmetry ($R\bar{3}c$) and cubic symmetry ($Pm\bar{3}m$) in the same nominal composition are very close at 800 °C (Figure 5a), implying a high probability of a reversible phase transformation $R\bar{3}c \leftrightarrow Pm\bar{3}m$ at high temperatures. This correlates with the dilatometry measurements. The linear thermal expansion of LNFM02, LSNFM10, and LSNFM20 shows the change in the slope between 530 and 600 °C (Table 4), which may be related to a phase transformation. The change in the thermal expansion coefficients (TEC) within the same temperature range and close TEC values observed on heating and cooling correlate with the reversible character of the high-temperature phase transition within the cation stoichiometric perovskite phase in the A-site deficient compositions. Beside, the perovskite phase with rhombohedral symmetry was observed in the XRD patterns recorded at room temperature initially (as synthesized) and after the high-temperature neutron diffraction study.

A high-temperature phase transition within the cation stoichiometric perovskite phase from rhombohedral ($R\bar{3}c$) to cubic symmetry ($Pm\bar{3}m$) occurs in all the nominal compositions investigated. The higher the level of Sr doping, the less the fraction of the perovskite constituent with cubic symmetry was (Figure 4b, at 800 °C). It could be related to the stabilization of the simple perovskite structure with rhombohedral distortions through the Sr doping that will be discussed in the next section. The results obtained in the present study demonstrate also that the concentration of the high temperature phase can be controlled through the different doping and not only through the variation in the external thermodynamic conditions (oxygen partial pressure).[11] The oxygen site occupancy in the phase with cubic structure ($Pm\bar{3}m$) was estimated to be complete within the detection limit of Rietveld analysis. One can assume that the high-temperature transition $R\bar{3}c \rightarrow Pm\bar{3}m$ could be initiated by low density of oxygen vacancies accompanied by the La and Sr cations redistribution within the perovskite structure. The lattice parameter of the high temperature perovskite phase with cubic symmetry ($Pm\bar{3}m$) increases with the rise in Sr and Mn substitution (Figure 5b). The distortions of the La/Sr−O_{12} polyhedra are very small. They increase slightly upon doping with Sr and Mn (Figure 8a). In contrast, the isotropic atomic displacements of La/Sr and O in the perovskite phase with the cubic symmetry ($Pm\bar{3}m$) are noticeably larger compared to Ni, Fe, and Mn (Figure 8b). The formation of the highly disordered high-temperature perovskite phase with cubic symmetry was observed for $CaTiO_3$.[19] The authors suggested that on approaching the transition temperature, the [TiO_6] octahedra become less distorted and their rotational disorder is reflected by the large atomic-displacement parameters of the oxygen.[19] The minimal deviation from the oxygen stoichiometry obtained from the refinement for the perovskite phase with cubic symmetry in the LSNFM series at 800 °C implies that all cations onto the B sublattice tend to exist in the oxidation state 3+ within a certain deviation, leading to more regular arrangement within the [Ni/Fe/MnO_6] octahedra and through the whole structure. To balance the difference in the ionic radii of Ni^{3+}, Fe^{3+}, and Mn^{3+} cations,[35] the isotropic displacements of La/Sr and O ions could occur simultaneously. Simultaneous observation of two opposite structural features (very small distortions of the La/Sr−O_{12} polyhedra and large isotropic atomic displacements of La/Sr cations) may imply synchronous scattering of La/Sr and O ions with B cations staying in the correct position through the perovskite structure.

Figure 6 illustrates the evolution of the lattice parameters and unit cell volume for the perovskite phase with rhombohedral symmetry ($R\bar{3}c$) in the LSNFM series. The change in the *a* lattice parameter and the unit cell volume upon doping with Sr and Mn obeys the Vegard's law over the whole temperature range investigated. The *a* lattice parameter and the unit cell volume increase linearly as a function of temperature, whereas the beta angle gradually decreases. The tilting of the [Ni/Fe/Mn]O_6 octahedra in the perovskite phase could lead to the deviation from the ideal cubic perovskite structure. The tilts in the perovskite with the rhombohedral symmetry ($R\bar{3}c$) occur about *a*, *b*, and *c* axes in antiphase. It can be represented as $\bar{a}\,\bar{a}\,\bar{a}$ in terms of the notation of Glazer.[36] The average tilting angle of the [Ni/Fe/Mn]O_6 octahedra, $\langle\omega\rangle$, can be defined as

$$\langle\omega\rangle = (180 - \langle \mathrm{Ni/Fe/Mn - O - Ni/Fe/Mn}\rangle)/2 \qquad (1)$$

where $\langle$Ni/Fe/Mn−O−Ni/Fe/Mn$\rangle$ is the average superexchange angle $\langle$Ni/Fe/Mn−O−Ni/Fe/Mn$\rangle$, which can be evaluated from the refinement of the crystal structure of the phase with rhombohedral symmetry. The average tilting angle is comparable for the perovskite phases ($R\bar{3}c$) in all the A-site deficient compositions and decreases gradually with the temperature (Figure 7a). The average Ni/Fe/Mn−Ni/Fe/Mn distances increase gradually upon doping and with the rise in the temperature (Figure 7b). The NPD data obtained in the present study do not allow us to distinguish the distortions of the

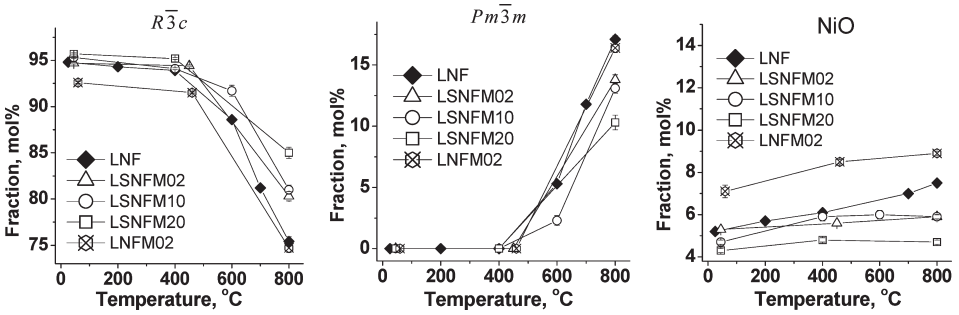

Figure 4. Fraction of different phases in the A-site deficient nominal compositions as a function of the temperature. The error bars are within the symbols.

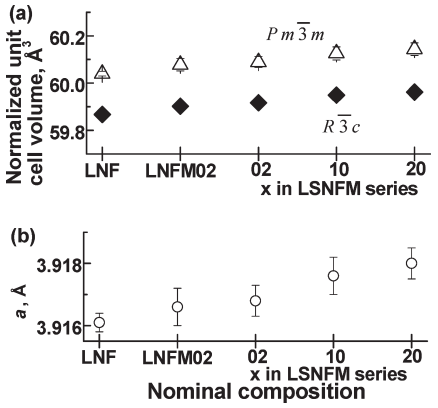

Figure 5. (a) Comparison of the normalized unit cell volumes for the cation stoichiometric perovskite phases with rhombohedral ($R\bar{3}c$) and cubic ($Pm\bar{3}m$) symmetries at 800 °C upon Sr and Mn doping and (b) the lattice parameter of the perovskite phase with cubic symmetry ($Pm\bar{3}m$). The error bars are within the symbols.

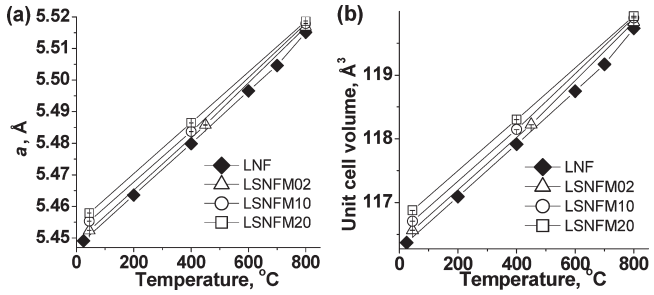

Figure 6. Evolution of (a) the *a* lattice parameter and (b) the unit cell volume of the cation stoichiometric perovskite phase with rhombohedral structure ($R\bar{3}c$) in the LSNFM series as a function of the temperature. The error bars are within the symbols.

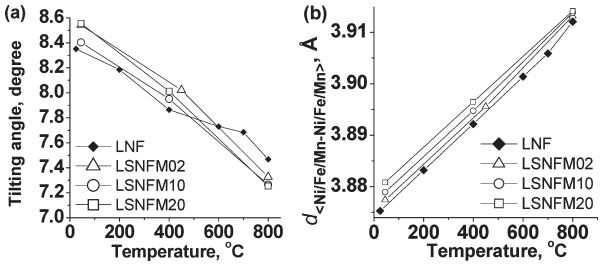

Figure 7. Evolution of (a) the $[Ni/Fe]O_6$ and $[Ni/Fe/Mn]O_6$ octahedra tilting angles and (b) the average Ni/Fe/Mn−Ni/Fe/Mn distances with the temperature for the cation stoichiometric perovskite phase with rhombohedral structure in the LSNFM series.

$[Ni/Fe/Mn]O_6$ octahedral cages, which are expected and could influence the electronic structure of the doped perovskite phases. In contrast, the distortions of the La/Sr−O_{12} polyhedra in the perovskite phase with rhombohedral symmetry ($R\bar{3}c$) were revealed. They decrease upon doping with Sr and Mn (Figure 8a). The isotropic displacement parameters for all ions in the perovskite phase with the rhombohedral symmetry ($R\bar{3}c$) are low (Figure 8c).

Information about the crystal structure of the compositions in the LSNFM series and the phase transformations observed under air with the temperature variation is summarized in Figure 9a.

3.4. NiO Exsolution from the Perovskite Structure and Extinction of A-Site Deficiency. The fraction of NiO obtained from the refinement was comparable with the nominal A-site deficiency in all the A-site deficient compositions explored (Table 1), indicating a very low range of A-site deficiency in the simple perovskite structure with Ni (high fraction), Fe, and Mn cations on the B-sublattice. The M−O bonds (M = W, Nb, Ta, Ti) in bronzes (Na_xWO_3), $La_{1/3}NbO_3$, $La_{1/3}TaO_3$, and $La_{2/3}TiO_3$ have a high degree of covalence, and stable M−O networks can be formed, within which La and Sr cations at the 12 coordinated A-sites can be missing. In contrast, Ni (2+, 3+), Mn (2+, 3+, and 4+), and Fe (2+, 3+, and 5+ in a small quantity) in the simple perovskites can easily change oxidation state, resulting in less stability of $[NiO_6]$, $[MnO_6]$, and $[FeO_6]$ octahedra and the whole simple perovskite structure. A steric effect associated with the difference in the ionic radii of Ni^{3+} and Ni^{2+} cations could be a reason resulting in the exsolution of NiO from the perovskite structure and the extinction of A-site deficiency. According to the refinement, the perovskite phase with rhombohedral symmetry shows a slight deviation from the oxygen stoichiometry in the temperature range of 45−460 °C (Table 2). The existence of the oxygen vacancies in the first coordination shell could be compensated through the generation of a small fraction of Ni^{2+} cations. $LaNiO_{3-\delta}$ perovskite shows the lowest thermochemical stability in air among the $LaBO_3$ perovskites (where B = Cr, Mn, Fe, Co, and Ni).[40] The average oxidation state of Ni cations in LNF is less than 3$^+$,[13] and it tends to reduce with the Mn substitution.[33] The effective ionic radius of Ni^{2+} is higher than for Ni^{3+} ($r^{VI}_{Ni^{2+}}$ = 0.70 Å; $r^{VI}_{Ni^{3+}(LS)}$ = 0.56 Å; $r^{VI}_{Ni^{3+}(HS)}$ = 0.60 Å), Fe, and Mn cations ($r^{VI}_{Mn^{3+}(LS)}$ = 0.58 Å; $r^{VI}_{Fe^{3+}(LS)}$ = 0.55 Å; $r^{VI}_{Fe^{2+}(LS)}$ = 0.61 Å),[35] resulting in the mismatch in the Ni^{2+}−O and Ni^{3+}(Mn^{3+},Fe^{3+})−O bond lengths within $[NiO_6]$ or adjusted $[Ni/Fe/MnO_6]$ octahedra.

dx.doi.org/10.1021/cm103486z |*Chem. Mater.* 2011, 23, 1841–1850

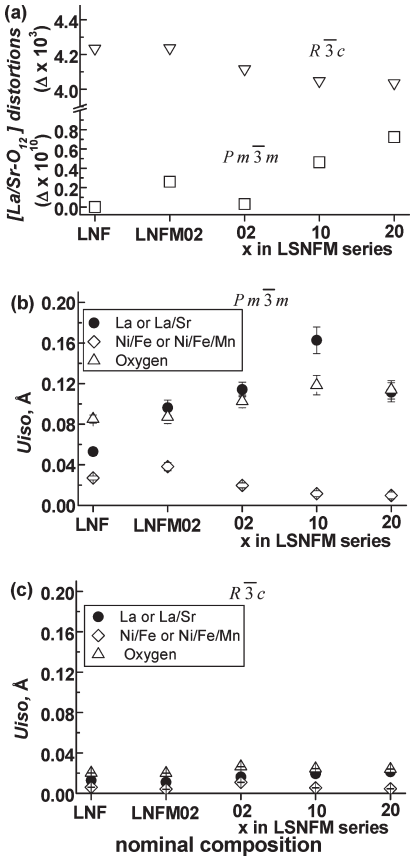

Figure 8. (a) Comparison of the La/Sr−O_{12} polyhedra distortions in the cation stoichiometric perovskite phases ($R\bar{3}c$ and $Pm\bar{3}m$) at 800 °C; Δ is a measure of the distortion of the La/Sr−O_{12} polyhedra with the average La/Sr−O distance $\langle d \rangle$ estimated as $\Delta = (1/N)\Sigma_{n=1,N}\{(d_n - \langle d \rangle)/\langle d \rangle\}^2$. Isotropic displacement parameters at 800 °C for the perovskite phases with (b) cubic symmetry ($Pm\bar{3}m$) and (c) rhombohedral symmetry ($R\bar{3}c$) in the A-site deficient compositions.

The presence of vacancies on the A-sublattice would create additional distortions through the simple perovskite structure. After reaching a certain degree of a local deformation within the [NiO_6] octahedra, which seems to be relatively low, the simple perovskite lattice could undergo structural transformations or start decomposing and forming NiO as a secondary phase. The NiO exsolution was reported earlier from the cation stoichiometric $LaFe_{0.6}Ni_{0.4}O_3$ after the high temperature treatment.[41] The refinements carried out indicate that the B-site deficiency is not favorable for the simple perovskite structure with Ni, Fe, and Mn onto the B sublattice, assuming that the exsolution of NiO from the perovskite lattice could be accompanied by the segregation of La_2O_3 or La related phases. Incorporation of strontium onto the A sublattice with a larger ionic radius ($r^{XII}_{Sr^{2+}}$ = 1.44 Å; $r^{XII}_{La^{3+}}$ = 1.32 Å)[35] could compensate local distortions caused by the reduction of Ni cations to lower oxidation state and the increase in the Ni^{2+}−O bond length within the octahedra, thereby stabilizing the perovskite structure with rhombohedral symmetry and minimizing the NiO exsolution. This correlates with the fact that the NiO exsolution from the perovskite structure with increasing temperature was stronger in LNFM02 and LNF compared to the Sr doped LSNFM compositions ($0.004 \leq x_{Sr} \leq 0.042$) (Figure 4c). Notice that LNF and LNFM02 have nearly the same values of the nominal A-site deficiency at room temperature (Table 1). The presence of Mn cations may also make the perovskite structure be more tolerant to the presence of Ni^{2+} cations compensating the local distortions within [NiO_6] octahedra through altering the length of the adjusted Mn^{n+}−O bonds. This seems to occur only if Sr cations exist within the perovskite structure because a similar amount of NiO (~2 mol %) exsolved additionally from the perovskite structure in LNF and LNFM02 with the rise in the temperature up to 800 °C.

3.5. Thermochemical Stability in Air. The Mn and Sr doped compositions exhibit good thermal stability in air (Figure 9b), implying that the overall oxygen stoichiometry is nearly constant with the temperature variation. This also presumes that a change in the oxidation state of Ni (as the most reducible) could be compensated through the increase in the oxidation states of Mn and Fe cations through the double exchange mechanism[34] or more complex interactions involving all three transition metal cations.

3.6. Conductivity in Air. The LSNFM compositions synthesized show complex conductivity behavior in air. The conductivity diagram for the LSNFM system is presented in Figure 9a. LSNFM02 exhibits metallic-like conductivity above 300 °C as LNF (Figure 9b). Metallic-like conductivity behavior becomes apparent in LSNFM10 above 640 °C, whereas LSNFM20 shows semiconducting behavior in a temperature range of 50−840 °C. The apparent activation energy slightly increases in the LSNFM series: 0.04 eV (50−300 °C) for LNF and LSNFM02, 0.07 eV (50−635 °C) for LSNFM10, and 0.09 eV (50−840 °C) for LSNFM20. Low values of the activation energy imply that the conductivity is electronic (not ionic), and small polaron conduction dominates. All the compositions investigated show semiconducting behavior at temperatures below 300 °C. The conductivity in the LSNFM series decreases gradually upon Sr and Mn doping, which correlates with the rise in the unit cell volume of the perovskite phases (Figures 6 and 9b). Comparison of the phase and conductivity diagrams of the LSNFM system (Figure 9a) illustrates that above 300 °C there is no correlation between the phase evolution and transport properties. For instance, at 800 °C, both LSNFM10 and LSNFM20 comprise the perovskite phase with rhombohedral symmetry ($R\bar{3}c$), the perovskite phase with cubic symmetry ($Pm\bar{3}m$), and NiO, but they show different types and values of conductivity (Figure 9b). The increase in the lattice parameters for the perovskite phases with rhombohedral and cubic structure upon Sr and Mn doping at 400 and 800 °C shows nearly the same trend as at room temperature (Figures 5b and 6). On the other hand, there is an important difference in the mechanism of electronic conductivity in ABO_3 perovskites (B = Mn, Fe, and Ni). For Mn and Fe containing perovskites, the small polaron hopping mechanism is dominant.[42,43] The small polaron band conduction was assumed for the perovskite phase in LNF at 500 °C.[12] In the case of the small polaron hopping conduction, the mobility of the charge carriers increases with the rise in the temperature, whereas in the case of the small polaron band conduction, the mobility of the charge carriers decreases with the increase in the temperature. The electronic conductivity (σ_e) is proportional to the number of charge carriers (n), their charge (e), and mobility (μ)

$$\sigma_e = n \times e \times \mu \qquad (2)$$

Therefore, the value of the mobility of the charge carriers can be evaluated for the perovskite phases with rhombohedral and cubic symmetries in the LSNFM compositions. In the case of the small polaron band conduction, only electrons related to Ni cations

Table 4. Linear Thermal Expansion Coefficient (TEC) in Air

composition	regime	TEC, K^{-1}	
[a]LNF	cooling	11.9×10^{-6} (300−550 °C)	13.4×10^{-6} (600−900 °C)
LNFM02	cooling	11.4×10^{-6} (300−555 °C)	12.7×10^{-6} (580−900 °C)
[b]LSNFM10	heating	$(11.5 \pm 0.1) \times 10^{-6}$ (300−530 °C)	$(12.0 \pm 0.1) \times 10^{-6}$ (560−900 °C)
	cooling	$(11.5 \pm 0.3) \times 10^{-6}$ (300−530 °C)	$(12.6 \pm 0.1) \times 10^{-6}$ (550−900 °C)
[b]LSNFM20	heating	$(12.5 \pm 0.4) \times 10^{-6}$ (300−580 °C)	$(13.9 \pm 0.1) \times 10^{-6}$ (600−900 °C)
	cooling	$(12.6 \pm 0.1) \times 10^{-6}$ (300−580 °C)	$(13.9 \pm 0.2) \times 10^{-6}$ (600−900 °C)

[a] From ref 11. [b] The average value of the two measurements.

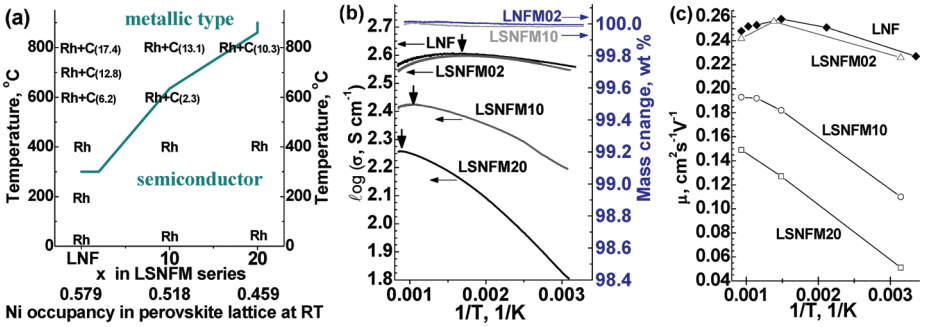

Figure 9. (a) phase and conductivity diagrams of the LSNFM system. Crystal symmetry: Rh, rhombohedral; and C, cubic. The numbers in the round baskets are the concentration of the perovskite phase with cubic symmetry; (b) temperature dependences of the electronic conductivity and thermochemical stability in the LSNFM series; and (c) temperature dependences of the mobility of the electronic charge carriers (assuming that electrons related only to Ni cations are involved in the conduction). $a(o_2) = 0.21$.

would be involved. Therefore, the numbers of carriers were obtained assuming that one electron per Ni cation is involved in the charge transfer process; the unit cell volume of the perovskite phases with rhombohedral symmetry (V_{rh}) or cubic symmetry (V_{cub}) contains 2 or 1 formula units (Z), respectively, and the Ni occupancy (f_{Ni}) onto the B sites varies depending on the doping regimes and temperature (Table 2):

$$n = (1 \times Z \times f_{Ni})/V \quad (3)$$

$$\mu = \sigma_e \times V/(1 \times Z \times f_{Ni} \times e) \quad (4)$$

Figure 9c illustrates the temperature dependences of the mobility of the charge carriers in the perovskite phases with rhombohedral symmetry. The same values of the mobility were obtained in the perovskite phases with rhombohedral and cubic symmetries at 800 °C. The value of the mobility ~0.1 $cm^2 \cdot s^{-1} \cdot V^{-1}$ is usually taken as the minimum value for the band conduction.[44] The values of the mobility calculated for the perovskite phases with different doping levels are higher compared to the limiting value (except LSMNF20 below 400 °C), but a nonlinear trend in the change of the mobility was observed for LNF, LSNFM02, and LSNFM10 with the increase in the temperature. For LSNFM02 and LNF, the mobility decreases in the temperature range of 400−800 °C, supporting the small polaron band conduction. The mobility of the charge carriers in LSMNF10 is nearly constant above 600 °C, probably representing the temperature range where the change from the small polaron hopping conduction to the small polaron band conduction occurs. The conduction band in LSNFM02, LSNFM10 (above 635 °C), and LNF may be formed through direct overlapping of the 3d Ni−3d Ni and 3d Ni−2p O orbitals. Because nearly the same values of the average tilting angles were observed for the perovskite phases with rhombohedral structure (Figure 7a), which is prevailing in the LSNFM series over the whole temperature range (Figure 4a), one can expect a minor contribution of the superexchange interactions via the oxygen (3d Ni−2p O−3d Ni) and assume that the conduction band is mainly formed by the direct overlapping of the 3d Ni−3d Ni orbitals. Metallic-like conductivity was observed in the substituted $LaNiO_3$ if the Ni occupancy on the B sublattice is higher than 50 mol % ($LaFe_{1-x}Ni_xO_3$ and $La_{0.9}Sr_{0.1}Ga_{1-x}Ni_xO_3$).[41,45] The continuousness of the 3d Ni−3d Ni band, in this case, would depend not only on the Ni−Ni bond length but also on the number of Ni neighbors. With the increase in the Mn substitution, it is reasonable expect a destruction of the 3d Ni−3d Ni band and switching to the small polaron hopping mechanism. In LSNFM10, the Ni occupancy of the B-site equals to 0.518−0.512 (45−800 °C), which is very close to 50%, and it exhibits semiconducting behavior below 635 °C. The Ni occupancy of the B-site in LSNFM20 is less than 50% (0.459−0.453 in the range of 45−800 °C), and LSNFM20 exhibits semiconducting conductivity over the same temperature range. Probably on heating, the continuousness of the 3d Ni−3d Ni band could be restored due to small changes in the electronic structure of the perovskite phase.

4. CONCLUSIONS

High-temperature neutron diffraction study reveals that the Mn and Sr doped A- site deficient $La_{0.95}Ni_{0.6}Fe_{0.4}O_3$ (LSNFM) can be represented as a mixture of a cation stoichiometric perovskite phase with rhombohedral structure and NiO in the temperature range of 45−460 °C. The cation stoichiometric perovskite phase undergoes the high temperature phase transition from rhombohedral ($R\bar{3}c$) to cubic ($Pm\bar{3}m$) symmetry

dx.doi.org/10.1021/cm103486z |Chem. Mater. 2011, 23, 1841–1850

above 530−600 °C, which could be triggered by a low density of the oxygen vacancies within the oxygen sublattice accompanied by a certain distribution of La and Sr cations within the A-sublattice. The increase in the Sr doping diminishes the exsolution of NiO from the perovskite structure and reduces the high-temperature phase transformation within the cation stoichiometric perovskite phase in the LSNFM series, demonstrating that the concentration of the high temperature phase can be controlled through the different doping regimes.

A low level of Mn doping ($z = 0.021$) results in the expansion of the perovskite lattice with rhombohedral and cubic symmetries, whereas a very low level of Sr doping ($x = 0.004$) leads to a minor effect. The *a* lattice parameter and the unit cell volume of the cation stoichiometric perovskite phase increase upon further doping with Sr and Mn in the LSNFM series, which could be related to the increase in the concentration of Sr cations with a larger ionic radius and the rise in the fraction of Ni^{n+} cations in a lower oxidation state.

The LSNFM compositions exhibit complex conductivity behavior upon Sr and Mn doping. At room temperature all the compositions show semiconducting behavior. The change in the electronic conductivity upon doping below 300 °C could be related to the expansion of the crystal lattice of the doped perovskite phase. The electronic conductivity in the A-site deficient nominal compositions does not follow the phase and structural evolution with the temperature variation. The change from the small polaron hopping mechanism to the small polaron band mechanism could occur in the LSNFM compositions with the rising temperature.

■ ASSOCIATED CONTENT

Supporting Information. Details on the samples fabrication. This material is available free of charge via the Internet at http://pubs.acs.org.

■ AUTHOR INFORMATION

Corresponding Author
*E-mail: elena.konysheva@googlemail.com.

■ ACKNOWLEDGMENT

The authors thank EPSRC for funding. We also gratefully acknowledge Dr. E Suard and Mr. L. Gendrin (ILL Grenoble) for help with neutron diffraction measurements.

■ REFERENCES

(1) Chiba, R.; Yoshimura, F.; Sakurai, Y. *Solid State Ionics* **1999**, *124*, 281.
(2) Jiang, S. P.; Love, J. G.; Zhang, J. P.; Hoang, M.; Ramprakash, Y.; Hughes, A. E.; Badwal, S. P. S. *Solid State Ionics* **1999**, *121*, 1.
(3) Kostogloudis, G. Ch.; Ftikos, Ch. *Solid State Ionics* **1999**, *126*, 143.
(4) Tao, S.; Irvine, J. T. S. *Nat. Mater.* **2003**, *2*, 320.
(5) Knudsen, J.; Friehling, P. B.; Bonanos, N. *Solid State Ionics* **2005**, *176*, 1563.
(6) Konysheva, E.; Laatsch, J.; Wessel, E.; Tietz, F.; Christiansen, N.; Singheiser, L.; Hilpert, K. *Solid State Ionics* **2006**, *177*, 923.
(7) Hansen, K. K. *J. Electrochem. Soc.* **2009**, *156*, B1257.
(8) Tao, S.; Irvine, J. T. S. *Chem. Mater.* **2006**, *18*, 5453.
(9) Striker, T.; Ruud, J. A.; Gao, Y.; Heward, W. J.; Steinbruchel, C. *Solid State Ionics* **2007**, *178*, 1326.
(10) Zheng, F.; Pederson, L. R. *J. Electrochem. Soc.* **1999**, *146*, 2810.
(11) Konysheva, E.; Suard, E.; Irvine, J. T. S. *Chem. Mater.* **2009**, *21*, 5307.
(12) Konysheva, E.; Irvine, J. T. S. *J. Power Sources* **2009**, *193*, 175.
(13) Konysheva, E.; Irvine, J. T. S. *J. Mater. Chem.* **2008**, *18*, 5147.
(14) Lunkenheimer, P.; Loidl, A.; Ottermann, C. R.; Bange, K. *Phys. Rev. B* **1991**, *44*, 5927.
(15) Duffy, D. M.; Tasker, P. W. *Philos. Mag.* **1984**, *50*, 143.
(16) Rao, C. N. R.; Gopalakrishman, J. *New directions in solid state chemistry*; Cambridge University Press: Cambridge, 1997; p 551.
(17) Rooksby, H. P.; White, E. A. D.; Langston, S. A. *J. Am. Ceram. Soc.* **1965**, *48*, 447.
(18) Abe, M.; Uchino, K. *J. Mater. Res. Bull.* **1974**, *9*, 147.
(19) Vogt, T.; Schmahl, W. W. *Europhys. Lett.* **1993**, *24*, 281.
(20) Knight, K. S. *Solid State Ionics* **1994**, *74*, 109.
(21) Slater, P. R.; Irvine, J. T. S.; Ishihara, T.; Takita, Y. *J. Solid State Chem.* **1998**, *139*, 135.
(22) Knizek, K.; Hejtmanek, J.; Jirak, Z.; Martin, C.; Hervieu, M.; Raveau, B.; André, G.; Bouree, F. *Chem. Mater.* **2004**, *16*, 1104.
(23) Gateshki, M.; Igartua, J. M.; Hernandez-Bocanegra, E. *J. Phys.: Condens. Matter* **2003**, *15*, 6199.
(24) Tichy, R. S.; Goodenough, J. B. *Solid State Sci.* **2002**, *4*, 661.
(25) Grenier, J.-C.; Ea, N.; Pouchard, M.; Hagenmuller, P. *J. Solid State Chem.* **1985**, *58*, 243.
(26) Hodges, J. P.; Short, S.; Jorgensen, J. D.; Xiong, X.; Dabrowski, B.; Mini, S. M.; Kimball, C. W. *J. Solid State Chem.* **2000**, *151*, 190.
(27) Aksenova, T. V.; Gavrilova, L. Ya.; Cherepanov, V. A. *Inorg. Mater.* **2004**, *40*, 1336.
(28) Aksenova, T. V.; Anan'ev, M. V.; Gavrilova, L. Ya.; Cherepanov, V. A. *Inorg. Mater.* **2007**, *43*, 296.
(29) Rietveld, H. M. *Acta Crystallogr.* **1967**, *22*, 151.
(30) Larson, A. C.; von Dreele, R. B. *GSAS - Generalised Structure Analysis System*; Los Alamos National Laboratory Report LAUR-86-748; Los Alamos National Laboratory: Los Alamos, NM, 1994.
(31) Konysheva, E.; Irvine, J. T. S. *Chem. Mater.* **2009**, *21*, 1514.
(32) NIST Centre for Neutron Research. http://www.ncnr.nist.gov/resources/n-lengths/elements (last excess October 2010).
(33) Sanchez, M. C.; Subfas, G.; Perez-Cacho, J.; Garcia, J.; Blasco, J. *J. Synchrotron Radiat.* **2001**, *8*, 901.
(34) Cox, P. A. *Transition Metal Oxides*; Clarendon Press: Oxford, 1995; p 283.
(35) Shannon, R. D.; Rewitt, C. T. *Acta Crystallogr., Sect. B* **1969**, *25*, 925.
(36) Glazer, A. M. *Acta Crystallogr., Sect. A* **1975**, *31*, 756.
(37) Salje, E. *Philos. Trans. R. Soc. London, Ser. A* **1989**, *328*, 409.
(38) Ritter, C.; Radaelli, P. G.; Lees, M. R.; Barratt, J.; Balakrishnan, G.; Paul, D. McK *J. Solid State Chem.* **1996**, *127*, 276.
(39) Howard, C. J.; Stokes, H. T. *Acta Crystallogr., Sect. B* **1998**, *54*, 782.
(40) Nakamura, T.; Petzow, G.; Gauckler, L. J. *J. Mater. Res. Bull.* **1979**, *14*, 649.
(41) Świerczek, K.; Marzec, J.; Pałubiak, D.; Zając, W.; Molenda, J. *Solid State Ionics* **2006**, *177*, 1811.
(42) Kuo, J. H.; Anderson, H. U.; Sparlin, D. M. *J. Solid State Chem.* **1990**, *87*, 55.
(43) Jung, W. H. *Phys. B: Condens. Matter* **2001**, *299*, 120.
(44) Bosman, A. J.; val Daal, H. J. *Adv. Phys.* **1970**, *19*, 1.
(45) Long, N. J.; Lecarpentier, F.; Tuller, H. L. *Electroceramics* **1999**, *3*, 399.